J|A|C|S
JOURNAL OF THE AMERICAN CHEMICAL SOCIETY

Article

pubs.acs.org/JACS

Electrocatalytic Oxidation of Glucose by Rhodium Porphyrin-Functionalized MWCNT Electrodes: Application to a Fully Molecular Catalyst-Based Glucose/O_2 Fuel Cell

Kamal Elouarzaki,[†] Alan Le Goff,[†] Michael Holzinger,[†] Jessica Thery,[‡] and Serge Cosnier*[,†]

[†]Département de Chimie Moléculaire UMR-5250, ICMG FR-2607, CNRS-Université Joseph Fourier, BP-53, 38041 Grenoble, France
[‡]LCI/DTNM/LITEN/CEA, 17 Av. des Martyrs, 38054 Grenoble, France

Supporting Information

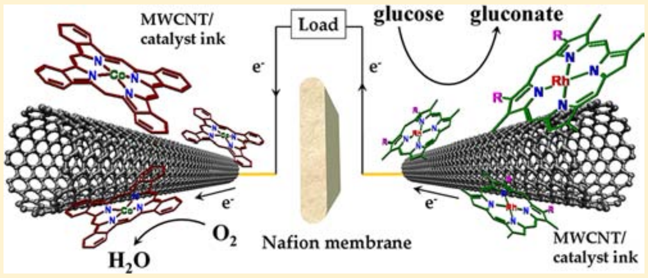

ABSTRACT: This paper details the electrochemical investigation of a deuteroporphyrin dimethylester (DPDE) rhodium(III) (**(DPDE)Rh^{III}**) complex, immobilized within a MWCNT/Nafion electrode, and its integration into a molecular catalysis-based glucose fuel cell. The domains of present **(DPDE)Rh^{I}**, **(DPDE)Rh–H**, **(DPDE)Rh^{II}**, and **(DPDE)Rh^{III}** were characterized by surface electrochemistry performed at a broad pH range. The Pourbaix diagrams (plots of $E_{1/2}$ vs pH) support the stability of **(DPDE)Rh^{II}** at intermediate pH and the predominance of the two-electron redox system **(DPDE)Rh^{I}**/**(DPDE)Rh^{III}** at both low and high pH. This two-electron system is especially involved in the electrocatalytic oxidation of alcohols and was applied to the glucose oxidation. The catalytic oxidation mechanism exhibits an oxidative deactivation coupled with a reductive reactivation mechanism, which has previously been observed for redox enzymes but not yet for a metal-based molecular catalyst. The MWCNT/**(DPDE)Rh^{III}** electrode was finally integrated in a novel design of an alkaline glucose/O_2 fuel cell with a MWCNT/phthalocyanin cobalt(II) (**CoPc**) electrode for the oxygen reduction reaction. This nonenzymatic molecular catalysis-based glucose fuel cell exhibits a power density of P_{max} = 0.182 mW cm^{-2} at 0.22 V and an open circuit voltage (OCV) of 0.64 V.

■ INTRODUCTION

Glucose is the most abundantly found monosaccharide in nature. Its complete oxidation can produce very high energy (-2.87×10^3 kJ mol^{-1}). To gain access to this amount of energy, direct conversion of chemical energy to electrical energy inside a glucose fuel cell is a promising alternative. There are two potential routes envisioned for the fabrication of the anode for efficient oxidation of glucose at low overpotentials: a metal or metal alloys electrode, operating mostly in an alkaline medium with compartmentalization of the electrodes,[1,2] and redox enzymes such as glucose oxidases or dehydrogenases,[3] operating at neutral pH without any compartmentalization. Enzyme electrodes take advantage of the selectivity of enzymes toward their substrates, but the difficult wiring of enzymes onto electrodes hinders the efficient electron transfer to the enzyme redox active site.[3−7]

In addition, enzyme electrodes suffer from the fragility of proteins immobilized in a nonbiocompatible microenvironment. The use of platinum and its alloys has been the electrochemical standard for oxygen reduction. It can achieve high catalytic efficiency and takes advantage of the well-known engineering process derived from polymer electrolyte membrane fuel cell (PEMFC).[1,8,9] However, metals are not ideal candidates for glucose fuel cell applications, being non-earth-abundant and nonrenewable, lacking substrate selectivity, and being easily poisoned in a complex medium. One other alternative to metals or enzymes is the use of molecular catalysts which mimic the enzymatic catalysis. The engineering of molecular electrocatalysts represents a promising route in the design of glucose fuel cells since it can potentially approach the efficiency and durability of a metal-based electrode, and the selectivity of the enzymatic reaction. While molecular catalysts such as cobalt porphyrins or copper complexes are already well described for the reduction of oxygen at the cathode,[10] only a few molecular catalysts have shown interesting catalytic properties toward the oxidation of glucose. Rhodium porphyrins recently appeared to show interesting overpotentials as highly efficient catalysts for the oxidation of glucose, taking advantage of its well-known properties for the homogeneous oxidative catalysis of alcohols in the presence of oxygen.[11] Of particular interest is the work carried out by L. Liu and co-workers where they investigate the mechanism of the oxidation of alcohols, using a water-soluble tetra *p*-sulfonatophenyl porphyrin rhodium(III) complex ((TSPP)Rh^{III}).[12] Electrochemical studies of rhodium porphyrins are mostly performed in DMSO, where such complexes are soluble, to address the intermediates in the reductive electrochemistry of (TPP)-

Received: May 11, 2012
Published: July 20, 2012

dx.doi.org/10.1021/ja304589m | *J. Am. Chem. Soc.* 2012, 134, 14078−14085

Rh^{III}.[13−15] Also, with the use of a carbon black as support, different types of Rh porphyrins achieve electrocatalysis of small substrates in water.[11,16−18] However, the intermediate oxidation states involved in electrocatalysis are not fully characterized. Since comprehensive understanding of the electrochemical characteristics of such Rh complexes are vital for its later use for energy conversion, we have elaborately investigated the electrochemical behavior of immobilized deuteroporphyrin dimethylester rhodium(III) complexes **(DPDE)Rh^{III}**. The immobilization on electrodes overcomes the issue of water insolubility and allows the stabilization of intermediary oxidation states at a controlled pH. In particular, we address the conditions of stability for the Rh^{II} porphyrin intermediate in water, which represents an important topic in the chemistry of rhodium complexes.[19,20]

Furthermore, we have chosen a multiwalled carbon nanotube (MWCNT)/Nafion-based electrode to optimize the electron transfers between the adsorbed complexes and the electrode. Due to the geometry of MWCNTs, this material has an enormous specific surface area and unique electrical and electrochemical properties. MWCNT-based electrodes have been proven to have excellent abilities as electrocatalytic support for both enzymes[3,21] and molecular catalysts.[22] Molecular electrocatalysts can easily be immobilized onto MWCNTs, in particular, by adsorption of π-extended systems such as porphyrins[23] or pyrene via $\pi-\pi$ interactions.[24] These nanohybrids exhibited promising electrocatalytic performances, in the replacement of carbon black associated to Pt catalyst for the oxygen reduction reaction.[10,23,25−27]

In this paper, we describe the fabrication and characterization of MWCNT/**(DPDE)Rh^{III}** electrodes. Cyclic voltammetry, performed at a broad of range of pH values, gives insights into the oxidation states of Rh porphyrin, immobilized on a MWCNT-based electrode, and also elucidates the particular mechanism of electrocatalytic glucose oxidation. The mechanism of electrocatalysis exhibits an original activation/deactivation mechanism for a molecular catalyst. This mechanism was first described by the Armstrong group while studying the mechanism of hydrogen oxidation of [NiFe] hydrogenases by protein film voltammetry.[28] This mechanism was further simulated through theoretical calculations by Limoges and Saveant,[29] and, more recently, by Leger and coworkers.[30] We have integrated the MWCNT/**(DPDE)Rh^{III}** hybrid electrode into a flow-through alkaline glucose/O_2 fuel cell. The latter constitutes the first example of an abiotic glucose/O_2 fuel cell fully based on molecular catalysts, namely **(DPDE)Rh^{III}** for the oxidation of glucose at the anode and cobalt phthalocyanin (**CoPc**) for the reduction of O_2 at the cathode.

■ EXPERIMENTAL SECTION

Materials. Commercially available reagents, cobalt(II) phthalocyanine, phosphoric acid (H_3PO_4), acetic acid (CH_3COOH), sulfuric acid (H_2SO_4), α-D-glucose, $Rh_2Cl_2(CO)_4$, Nafion, 1-methyl-2-pyrrolidinone (NMP), and potassium hydroxide (KOH) were of analytical grade and purchased from Sigma-Aldrich. Boric acid (H_3BO_4) was supplied by Euromedex. Commercial grade thin multiwalled carbon nanotubes (MWNTs) (9.5 nm diameter, purity >95%), obtained from Nanocyl, were used as received without any purification step. Deuteroporphine IX dimethyl ester was purchased from ABCR. All other reagents, solvents, acids, and bases were of special grade and were used without further purification. NMR spectra were recorded on a Bruker AVANCE 400 operating at 400.0 MHz for ^1H. ESI mass spectra were recorded with a Bruker APEX-Qe ESI FT-ICR mass spectrometer. UV−vis spectra were recorded with a Cary 1 spectrophotometer with a quartz cuvette (1 cm depth).

Deuteroporphyrine IX dimethyl ester rhodium(III) (**(DPDE)Rh^{III}**) was prepared and characterized according to the literature[11] and characterized by electrospray ionization mass spectrometry (ESI-MS), UV−vis spectroscopy (complete metalation was checked by disappearance of the Q-band), and ^1H NMR.

^1H NMR ($CDCl_3$): δ 10−10.15 (3s, 4H), 9.1 (s, 2H), 4.28 (t, 4H), 3.7 (s, 6H), 3.6 (s, 6H), 3.52 (s, 6H), 3.15 (t, 4H). UV−vis ($CHCl_3$) λ_{max}/nm (ε mM^{-1} cm^{-1}): 401 (127), 516 (16.3), 548 (24.6). ESI-MS m/z (in ethanol): 639.0 $[(DPDE)Rh^{III}]^+$, 667.0 $[(DPDE)Rh^{III})(CO)]^+$.

General Methods. Ultrapure water was obtained from a Milli-Q Purelab UHQ (Elga) with a resistivity of 18.2 MΩ/cm. The pH values of a solution were determined by a pH-meter (GLP, CRISON) equipped with a pH combination electrode. The pH meter was calibrated relative to standard phthalate (pH 4.0) and phosphate (pH 7.01 and 9.21) and buffer solutions prior to each use.

Electrochemical measurements were performed at 25 °C with an Autolab electrochemical analyzer (Eco Chemie, Utrecht, The Netherlands) controlled by GPES software (Eco Chemie).

Electrochemical Measurements. Cyclic voltammetry (CV) was performed in a conventional three-electrode cell equipped with a glassy carbon (GC) electrode (geometric area = 0.071 cm^2), a platinum wire counterelectrode, and a saturated calomel electrode (SCE) as reference electrode. The surfaces of GC electrodes were polished with a 2 μm diamond paste purchased from Presi (France), washed with water using ultrasound, and rinsed with acetone and ethanol.

Cyclic voltammograms (CVs) were recorded after three successive reproducible scans. Electrochemical experiments were performed in aqueous KOH solutions in the pH range 14 < pH < 13, 0.1 M. Britton−Robinson buffer solutions ($[CH_3COOH]$ = 0.1 M, $[H_3PO_4]$ = 0.1 M, $[H_3BO_4]$ = 0.1 M) were used in the pH range 2 < pH < 12.5, and aqueous H_2SO_4 solutions in the pH range 0 < pH < 1.5. The pH of a solution was changed by titration using aqueous KOH solutions. pH measurements were conducted during all experiments. All $E_{1/2}$ values reported in this work were determined from cyclic voltammogram as an average of the oxidative and reductive peak potentials ($E_{p,a}$ + $E_{p,c}$)/2. The solutions were deoxygenated by purging with argon prior to each experiment, and an argon flow was kept over the solution during the whole experiment.

Fabrication of MWCNT/(DPDE)Rh^{III} Electrode. MWCNT/**(DPDE)Rh^{III}** electrodes were fabricated using the following procedure: MWCNTs (5 mg) were added to 1 mL of NMP solvent containing 1 mg of the **(DPDE)Rh^{III}** complex and 5 μL Nafion. The suspension was homogenized by an ultrasonic generator for 30 min. The resulting supernatant was used as catalyst ink. For electrochemical investigations, a portion (10 μL) of this suspension was dropped onto a freshly polished GC disk electrode (3 mm diameter), and the solvent was removed under reduced pressure. For glucose fuel cell experiments, the catalytic inks, **CoPC**/MWCNTs at the cathode and **(DPDE)Rh^{III}**/MWCNTs at the anode, were, respectively, deposited on the anodic and cathodic compartments, separated by a Nafion 115 membrane, using a micropipet. The catalysts were deposited at a temperature of 50 °C. Solvents were removed at 100 °C under vacuum. The 250 nm thick gold collectors were then deposited via magnetron sputtering on both the anode and cathode for optimal electron collection. The fuel cell was then stuck on a polycarbonate sealed frame. The glucose solution is injected in the anodic compartment at constant flow (5 mL min^{-1}) using a peristaltic pump. There were 0.5 M glucose/0.5 M NaOH solutions used. The cathodic compartment was exposed to air under "breathing" conditions. The active area of the fuel cell is of 5.76 cm^2. The fuel cells are tested in ambient conditions at 20 °C.

Ink Composition. The compositions were as follows: **CoPC** on MWCNTs, 6.26 μmol of **CoPc** on 20 mg MWCNTs (1 mL deposited); **(DPDE)Rh^{III}** on MWCNTs, 6.26 μmol of **(DPDE)Rh^{III}** on 20 mg MWCNTs (1 mL deposited)

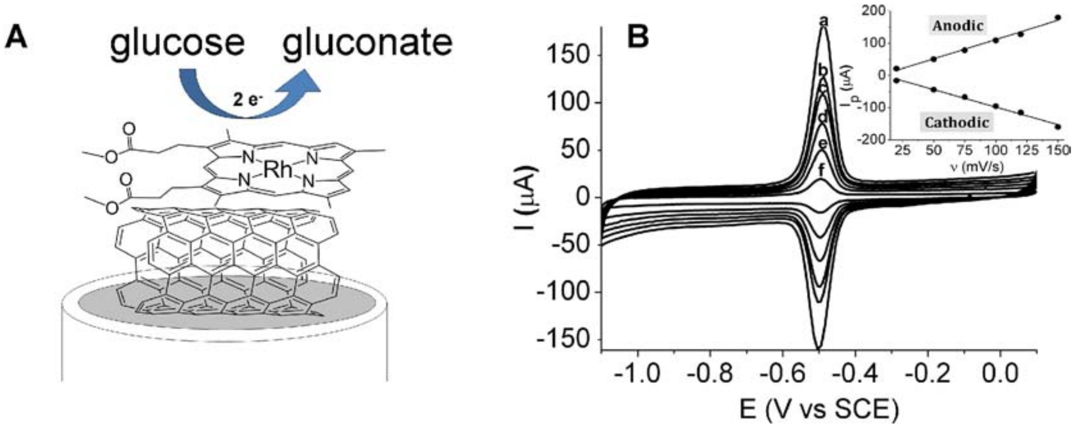

Figure 1. (A) Schematic representation of the MWCNT/(**DPDE**)**Rh**^{III} electrode. (B) Cyclic voltammetry of MWCNT/(**DPDE**)**Rh**^{III} electrode at different scan rates: (a) 150, (b) 125, (c) 100, (d) 75, (e) 50, and (f) 25 mV/s. The measurements were performed in 1 M KOH solution (pH 14). (Inset) Plot of peak currents vs scan rate.

■ RESULTS AND DISCUSSION

1. Characterization of the MWCNT/(DPDE)Rh(III) Electrodes. The catalyst ink is obtained by mixing MWCNTs with (**DPDE**)**Rh**^{III} and Nafion and dispersing the mixture in NMP using ultrasound for 30 min. This ink can be drop-casted either onto the GC electrode for the electrochemical analysis or onto the Nafion membranes during the fuel cell fabrication.

Modified GC electrodes were characterized by cyclic voltammetry. Figure 1 displays the electrochemical behavior of adsorbed (**DPDE**)**Rh**^{III} in KOH at pH 14. One single reversible redox system is observed at $E_{1/2} = -0.49$ V. CV scans performed at different scan rates showed a linear dependence of both oxidation and reduction currents with the scan rate (inset, Figure 1) which is characteristic for immobilized redox species. The width of the peak at half-height [$E_p^{ox}/2 = 50$ mV, $E_p^{red}/2 = 45$ mV at 20 mV s^{-1}] is close to the theoretical value of $90/2 = 45$ mV for a redox system involving two electrons. This confirms the excellent electron transfer between adsorbed (**DPDE**)**Rh**^{III} and MWCNTs.

A surface concentration of 6×10^{15} molecules cm^{-2} (geometrical surface 0.07 cm^2) was determined by integration of the oxidation (or reduction) peak. To estimate the number of porphyrin layers on the CNT walls, we estimated the electroactive surface of MWCNTs by using a redox probe, $Ru(NH_3)_6^{2+/3+}$. CV experiments at the Nafion−CNT/GC electrode were performed in 1 mM $Ru(NH_3)_6^{2+/3+}$ in 0.1 M KCl solution at various scan rates. From the slope of the linear curve and according to the Randles Sevick equation, the MWCNT electrodes exhibit an electroactive area of 1.2 cm^2, corresponding to a 17-fold increase compared to the geometrical area of 0.07 cm^2. The surface concentration of (**DPDE**)**Rh**^{III} thus corresponds to 3.5×10^{14} molecules cm^{-2} on the surface of the Nafion−CNT/GC electrode. It has been reported that the surface coverage of porphyrins in self-assembled monolayers was in the range of 20×10^{13} molecules cm^{-2}, in the particular case where all porphyrins are parallel on the electrode surface.[31] From this model, and considering that the parallel orientation of porphyrins are favored on CNT walls, we estimated the surface coverage of porphyrins groups on the surface of MWCNTs to approximatively 2 layers of (**DPDE**)**Rh**^{III}.

2. Potential−pH Diagram for (DPDE)Rh: Rh(I), Rh(II), and Rh(III) Domains. To get more insights into the oxidation states of rhodium involved in the molecular surface electrochemistry of (**DPDE**)**Rh**^{III} and its electrocatalytic properties, we have examined the cyclic voltammetry of MWCNT/(**DPDE**)**Rh**^{III} electrode over a broad range of pH values. Wayland et al. reported a well described equilibrium in solution for water-soluble (TSPP)Rh^{III} and related species.[32] In water, (TSPP)Rh^{III} exists as rhodium(III) diaquo complex in equilibrium with the mono- and bis-hydroxo complex, $[(TSPP)Rh^{III}(OH)(H_2O)]^{4-}$ and $[(TSPP)Rh^{III}(OH)_2]^{5-}$.

$$\begin{aligned}&(TSPP)Rh^{III}(OH)_2{}^{5-}\\&\quad \rightleftharpoons (TSPP)Rh^{III}(OH)(H_2O)^{4-}\\&\quad \rightleftharpoons (TSPP)Rh^{III}(H_2O)_2{}^{3-}\end{aligned}$$

The (TSPP)Rh^{I} species exist as the free (TSPP)Rh^{I} and its acid form, the Rh-hydride (TSPP)Rh−H.

$$(TSPP)Rh^{I}(H_2O)^{5-} \rightleftharpoons (TSPP)Rh(H)(H_2O)^{4-}$$

The (TSPP)Rh^{II} only exists at intermediate pH since (TSPP)Rh^{II} disproportionates at low and high pH values.

$$\begin{aligned}&(TSPP)Rh^{II}(H_2O)_2{}^{8-} + H^+ + H_2O\\&\quad \rightleftharpoons (TSPP)Rh^{I}(H)(H_2O)^{4-} + (TSPP)Rh^{III}(H_2O)_2{}^{3-}\end{aligned}$$

$$\begin{aligned}&[(TSPP)Rh^{II}(H_2O)]_2{}^{8-} + OH^-\\&\quad \rightleftharpoons (TSPP)Rh^{I}(H_2O)^{5-} + (TSPP)Rh^{III}(OH)(H_2O)^{4-}\end{aligned}$$

Here, we examined the electrochemical behavior of the (**DPDE**)**Rh**^{III} immobilized onto the MWCNT electrode and observed a pH dependence behavior for the redox couples involved in the surface electrochemistry of (**DPDE**)**Rh**^{III}.

In order to perform a systematic analysis of these features, CVs were acquired from pH 0 to 14 by employing a Britton−Robinson electrolyte buffer (Figure 2). Three main redox behaviors were observed using cyclic voltammetry.

For pH values between 14 and 12.5, the initial two-electron redox potential at pH 14 (−0.49 V) decreases with decreasing pH and splits to two one electron redox waves at −0.57 V and −0.44 V at pH 13. The redox potentials of these two redox systems are positively shifted with decreasing pH and correspond to two monoelectronic redox systems. This likely arises from the stabilization of a Rh^{II} species at intermediate pH, as has already been shown in solution.[32] Since the Rh(II) complex is immobilized on the electrode, we consider that

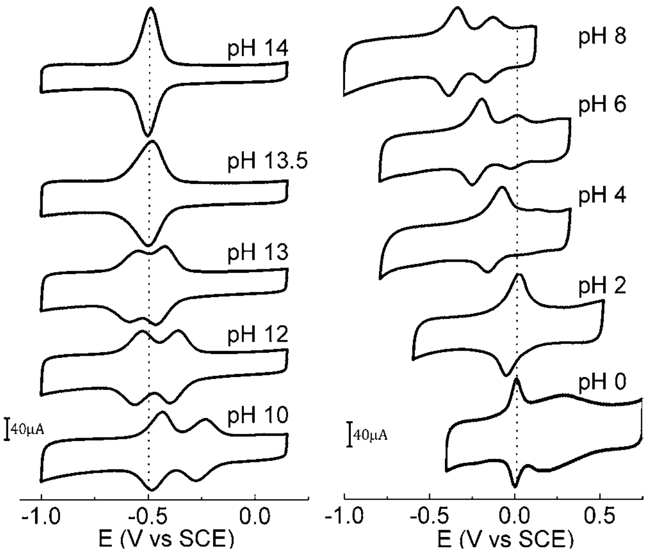

Figure 2. Cyclic voltammetry of the MWCNT/(**DPDE**)**Rh**$^{\mathrm{III}}$ electrode performed from pH 14 to pH = 0 (v = 50 mV s^{-1}, Britton–Robinson buffer, 25 °C).

dimerization is not likely in this particular case. The existence of the Rh(II) intermediate is confirmed by half width for both peaks of 105 mV which is close to the theoretical value of 90 mV. The variation of potential of this two monoelectronic redox system, corresponding to the (**DPDE**)**Rh**$^{\mathrm{II}}$/(**DPDE**)**Rh**$^{\mathrm{I}}$ and (**DPDE**)**Rh**$^{\mathrm{III}}$ /(**DPDE**)**Rh**$^{\mathrm{II}}$ couples, was plotted as a function of pH in an apparent Pourbaix diagram (Figure 3).

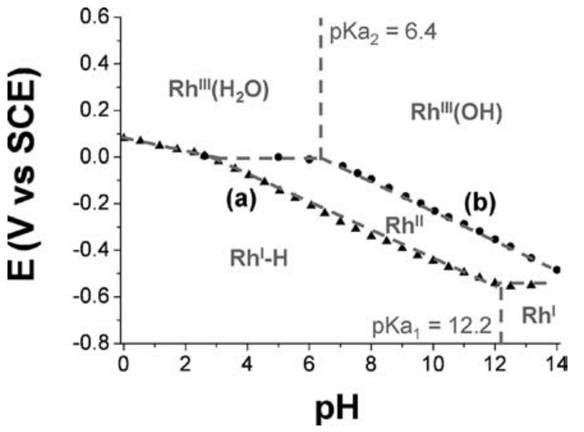

Figure 3. Apparent Pourbaix diagram (plots of $E_{1/2}$ (V vs SCE) vs pH) for the pH dependence of reversible oxidation of Rh(I) (▲, curve a) and Rh(II) (●, curve b) for the immobilized (**DPDE**)**Rh**$^{\mathrm{III}}$ complex in aqueous solution (T = 25 °C). The redox waves of the **DPDE** ligand and aqua ligand and charges are omitted for clarity. pK_{a1} and pK_{a2} correspond to the (**DPDE**)**Rh**$^{\mathrm{I}}$**-H**/ (**DPDE**)**Rh**$^{\mathrm{I}}$ and (**DPDE**)-**Rh**$^{\mathrm{III}}$(**H**$_2$**O**)/(**DPDE**)**Rh**$^{\mathrm{III}}$(**OH**) equilibria, respectively.

To discriminate any effect of coordination of buffer components, it is noteworthy that we did not observe any effect of the nature of buffer (NaOH, PBS or Britton–Robinson) at identical pH values on the shape of cyclic voltammograms.

Two curves were obtained corresponding to the potential variation observed in cyclic voltammetry (Figure 2). Both slopes could be fitted using the Nernst law

$$E = E^{\circ\prime} + 2.3RT/nF \times \log(1 + a_{\mathrm{H+}}/K_{\mathrm{Rh}})$$

where R is the gas constant, T the absolute temperature, and n is the number of exchanged electrons. $a_{\mathrm{H+}}$ is the proton activity measured from pH, K_{Rh} is the proton dissociation constant, and $E^{\circ\prime}$ is the apparent standard potential of the redox forms of Rh involved in the equation.

Curve a corresponds to the oxidation of (**DPDE**)**Rh**$^{\mathrm{I}}$ and can be divided into three sections with different slopes. The section at higher pH values (pH ≥ 12.2) implies a proton-coupled redox reaction for which the proton/electron stoichiometry is 0 (slope = 0), while in the pH range 2.8 < pH < 12.2, the stoichiometry is 1 (slope = 0.059), and at lower pH values (pH ≤ 2.8), the stoichiometry is 0.5 (slope = 0.029).

Curve b corresponds to the oxidation of (**DPDE**)**Rh**$^{\mathrm{II}}$ to (**DPDE**)**Rh**$^{\mathrm{III}}$ and can be divided into two sections. The first section above pH = 6.4 exhibits a slope of 0.064 corresponding to a one electron/one proton exchange while the second section below pH = 6.4 exhibits a slope equal to zero corresponding to a pH-independent electron transfer.

The apparent Pourbaix diagram clearly indicates the acid–base equilibrium of (**DPDE**)**Rh**$^{\mathrm{III}}$ in water and the redox potential measured by CV for the reversible systems, corresponding to the oxidation states of the (**DPDE**)**Rh**$^{\mathrm{III}}$ catalyst. Taking into account that these calculations were made for immobilized redox species, i.e., at the solid–liquid interface, they correspond only approximately to a real E–pH diagram for redox species in solution. This apparent Pourbaix diagram is illustrated by dotted lines in Figure 3. By fitting of the curves in the range 0 < pH < 14 in water, the domains of the present redox states of immobilized (**DPDE**)**Rh**$^{\mathrm{III}}$ and its electrochemical parameters could have been fully characterized. The parameters are summarized in Table 1.

The initial two-electron system at pH 14 is ascribed to (**DPDE**)**Rh**$^{\mathrm{III}}$ /(**DPDE**)**Rh**$^{\mathrm{I}}$ redox couple, while the first one-electron reduction process is assigned to the (**DPDE**)**Rh**$^{\mathrm{III}}$/(**DPDE**)**Rh**$^{\mathrm{II}}$ redox couple and the second one-electron reduction process is ascribed to the (**DPDE**)**Rh**$^{\mathrm{II}}$/(**DPDE**)**Rh**$^{\mathrm{I}}$ redox couple. Fitting curve a allows the determination of pK_{a1} = 12.2 for the (**DPDE**)**Rh**$^{\mathrm{I}}$**-H**/(**DPDE**)**Rh**$^{\mathrm{I}}$ equilibrium. The basic character of the rhodium hydride is in agreement with the pK_{a} measured for (TSPP)Rh(I) in water (pK_{a} = 8)[32] and (TPP)Rh(I) in DMSO (pK_{a} = 11).[33] Below pH 12.2, the characteristic slopes of 0.059 V per pH unit for both curve a and curve b indicate the concomitant exchange of one proton and one electron corresponding to the frontier between (**DPDE**)**Rh**$^{\mathrm{I}}$**-H**, (**DPDE**)**Rh**$^{\mathrm{II}}$, and (**DPDE**)**Rh**$^{\mathrm{III}}$(**OH**). For curve b, the inflection of the curve corresponding to a redox system independent of pH allows the determination of the apparent pK_{a} for the (**DPDE**)**Rh**$^{\mathrm{III}}$(**H**$_2$**O**)/ (**DPDE**)**Rh**$^{\mathrm{III}}$(**OH**) at pK_{a2} = 6.4. The acid–base equilibrium is close to the pK_{a} value of the water-soluble (TSPP)Rh$^{\mathrm{III}}$ in solution (pK_{a} = 7.85).[32] We therefore conclude that (**DPDE**)**Rh**$^{\mathrm{III}}$(**OH**)$_2$ species is most likely too basic to be observed in the presented pH range.

At decreasing pH values below 4, the redox system corresponds to the oxidation of (**DPDE**)**Rh**$^{\mathrm{II}}$ to (**DPDE**)**Rh**$^{\mathrm{III}}$ and exhibits a drastic decrease. The first oxidation corresponding to the oxidation of (**DPDE**)**Rh**$^{\mathrm{I}}$ to (**DPDE**)**Rh**$^{\mathrm{II}}$ is replaced by a redox system corresponding to a two-electron system as confirmed by the half width of 60 mV measured at pH = 0 (Figure 2). The latter finally becomes predominant at acidic pH, and its redox potential is positively shifted for decreasing

Table 1. Fitted Electrochemical Parameters for the pH Dependence of Immobilized DPDE−Rh Complex

pH range	protons/electrons	fitting equation	1/2 equation/apparent standard potential
		Curve a	
14−12.2	0/1	$E = -0.56$	$Rh^{I} = Rh^{II} + e^{-}/E^{\circ\prime} = -0.56$ V
12.2−2.8	1/1	$E = 0.15 - 0.059pH$	$Rh^{I}{-}H = Rh^{II} + e^{-} + H^{+}/E^{\circ\prime} = 0.15$ V
2.8−0	1/2	$E = 0.08 - 0.029pH$	$Rh^{I}{-}H = Rh^{III}(H_2O) + 2e^{-} + H^{+}/E^{\circ\prime} = 0.08$ V
		Curve b	
14−6.4	1/1	$E = 0.42 - 0.064pH$	$Rh^{II} = Rh^{III}(OH) + e^{-} + H^{+}/E^{\circ\prime} = -0.42$ V
6.4−2.8	0/1	$E = 0.00$	$Rh^{II} = Rh^{III}(H_2O) + e^{-}/E^{\circ\prime} = 0.00$ V

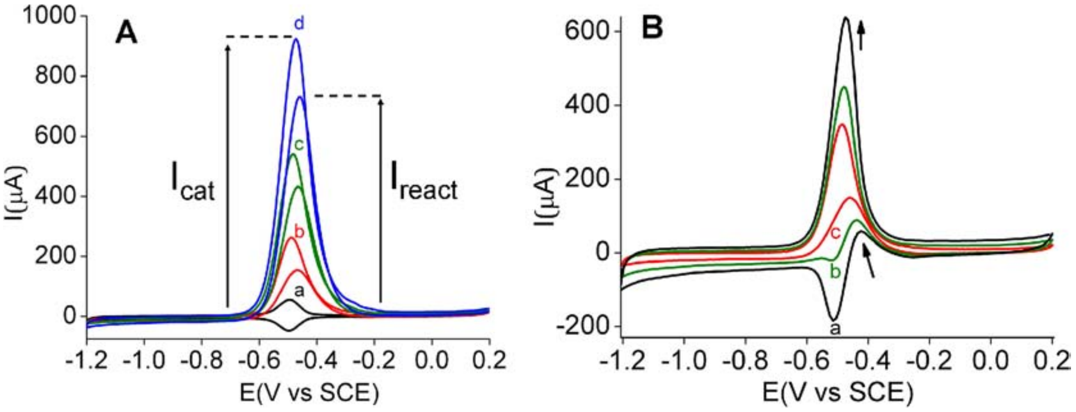

Figure 4. (A) Cyclic voltammograms of MWCNT/(**DPDE**)**Rh**^{III} electrode at a scan rate of 10 mV s^{-1} in the presence of (a) 0 mM, (b) 50 mM, (c) 150 mM, and (d) 250 mM glucose [measurements were performed in 1 M KOH (pH = 14) solution under a nitrogen atmosphere at 25 °C]. (B) Cyclic voltammograms of MWCNT/(**DPDE**)**Rh**^{III} with 50 mM of glucose obtained at different scan rates (a) 100 mV s^{-1}, (b) 50 mV s^{-1}, and (c) 20 mV s^{-1} (supporting electrolyte: 1 M KOH, pH = 14).

pH values with a slope of 0.029. This confirms the characteristic two electron redox system accompanied with one proton transfer, corresponding to the (**DPDE**)**Rh**^{III}(**H**$_2$**O**)/(**DPDE**)-**Rh**^{I}-**H** redox couple.

This Pourbaix diagram allows us to estimate the stable domains of (**DPDE**)**Rh**^{II} at intermediate pH. We have clearly determined the oxidation states of supported rhodium porphyrins involved in electrocatalytic mechanisms, especially for the oxidation of alcohols.

3. Mechanistic Insights into the Electrocatalytic Oxidation of Glucose by (DPDE)Rh^{III}. Rhodium porphyrins oxidize alcohols in basic conditions to enable the coordination of the alkylalcoholates to rhodium. The binding of primary and secondary alcohols to Rh^{III} triggers the β-elimination of hydrogen and the formation of a rhodium hydride that is subsequently deprotonated at basic pH to form Rh^{I}.[12] Rh^{I} is then chemically, via reaction with O_2, or electrochemically oxidized to regenerate the Rh^{III} catalyst. All experiments were performed under nitrogen to avoid reaction of Rh^{I} with O_2.

The cyclic voltammograms at different glucose concentrations are displayed in Figure 4 and Figure S3. It is noteworthy that MWCNT electrodes without Rh^{III} catalyst did not show any electrocatalytic activity toward glucose oxidation as shown on the CV in Figure S3.

Upon addition of glucose, the increase of the intensity of the peak at $E_{1/2} = -0.49$ V corresponds to the oxidation of (**DPDE**)**Rh**^{I} to (**DPDE**)**Rh**^{III}(**OH**) at pH = 14. This confirms the occurrence of electrocatalytic oxidation of glucose by the immobilized (**DPDE**)**Rh**^{III}. (**DPDE**)**Rh**^{I} is oxidized into (**DPDE**)**Rh**^{III} that reacts with glucose to give the hydride (**DPDE**)**Rh-H** and deprotonates rapidly at this pH to regenerate the (**DPDE**)**Rh**^{I} catalyst. While expecting an irreversible oxidation peak, we observed that the electrocatalytic waves exhibit a rare sharp twisted shape, i.e., a current decrease at higher overpotential and a current intensity recovery upon reversed scan. This behavior corresponds to an electrocatalytic deactivation occurring at increased overpotentials which is followed, on the reverse scan, by a regeneration of the catalyst at a redox potential close to the redox potential of the (**DPDE**)**Rh**^{III}/(**DPDE**)**Rh**^{I} couple. This regeneration triggers the reactivation of the electrocatalysis represented by the anodic current on the reverse scan.

To further study this activation/deactivation mechanism, the height of the reverse oxidation peak (I_{react}) was compared to the initial oxidation peak (I_{cat}). The ratio I_{react}/I_{cat} of the peak current, corresponding to the reactivation, and the peak current, corresponding to the initial catalysis, was taken as witness for the efficiency of the catalyst recovery through reductive scanning. We performed CV scans by varying both the concentrations of glucose and the scan rates (Figure 4A,B). The I_{react}/I_{cat} ratio toward the scan rates at different concentrations of glucose is depicted in Figure 5.

The reverse scans (Figure 4B), recorded at different scan rates, show the reactivation intensity decreases with scan rate. At fast scan rate (100 mV s^{-1}), the oxidation of (**DPDE**)**Rh**^{I} becomes reversible, with the electrochemical reduction peak of (**DPDE**)**Rh**^{III} being observed. Moreover, the plot of the ratio I_{react}/I_{cat} at different glucose concentrations shows that I_{react}/I_{cat} tends to zero at high scan rates. This confirms a slow recovering of the Rh(I) catalyst on the reverse scan at high scan rates. This confirms that the electrochemical reduction of Rh(III) is favored at higher scan rates compared to the chemical reduction by glucose.

From the CV investigations at increasing glucose concentrations and from the evolution of I_{react}/I_{cat} toward glucose, it can be stated that at higher glucose concentrations, the I_{react}/I_{cat}

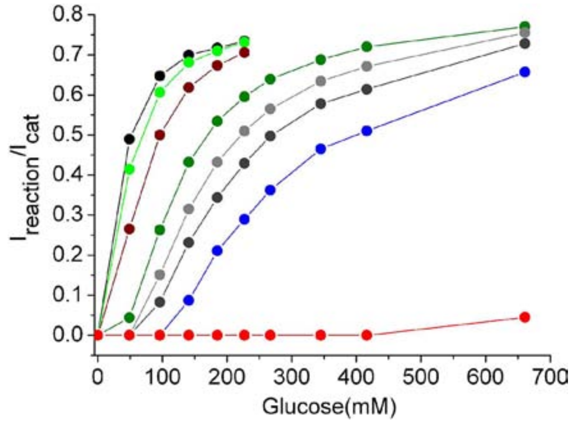

Figure 5. Plot of the ratio I_{react}/I_{cat} toward concentration of glucose at different scan rates: 5 (black), 10 (light green), 20 (brown), 50 (dark green), 75 (gray), 100 (dark gray), 150 (blue), 500 (red) mV s^{-1}.

ratio increases. This indicates that the recovery of the catalytic Rh^I intermediate is more efficient at higher concentrations of glucose. This phenomenon arises from the competitive behavior between the coordination of glucose and formation of the inactivated species.

This deactivation process was also confirmed by chronoamperometric measurements, performed at different potentials (Figure S1). The chronoamperogram, recorded at −0.6 V, corresponding to the foot of the catalytic oxidation wave, i.e., where no deactivation occurs, shows an almost constant current of 0.5 mA cm^{-2}. As observed for the CV scans, the deactivation rate is strongly dependent on the applied potential. The chronoamperometry, performed at higher overpotentials for instance at −0.48 V (the top of the catalytic peak), shows a high initial catalytic current of 3 mA cm^{-2} which decreases exponentially over time. Using the surface concentration of the catalyst [6×10^{15} molecules cm^{-2}] affords a maximum turnover number of 260 achieved within 1000 s.

This oxidative activation/reductive deactivation mechanism has previously been observed in redox enzymes. F.A. Armstrong and co-workers observed such a mechanism during the oxidation of H_2 by [NiFe] hydrogenases.[28] Saveant and Limoges deeply studied this so-called twisted reverse trace by theoretical calculations,[29] and more recently, Leger et al. simulated such a mechanism using a "two step" chronoamperometric method.[30] This rare behavior can only be observed when the oxidation of the catalytic site involves the competition between an active and an inactive form. In case of enzymes, this inactivation process could only be measured at low scan rates where enough time is given to induce the inactivation process. From the experimental data, the formation of a nickel-hydroxide, the inactivated form of the [NiFe] center of hydrogenases, was finally hypothesized. In our case, the deactivation is highly efficient as confirmed by the sharp oxidation peaks in the presence of glucose. According to the potential−pH diagram, (**DPDE**)**Rh**^{III}(**OH**) is responsible for the inactivation of the catalytic oxidation of glucose. At pH values where the oxidation of glucose is catalyzed, (**DPDE**)**Rh**^{III} exists as its hydroxide form in equilibrium with the glucose-coordinated form.[11] During the oxidation of (**DPDE**)**Rh**^{I}, the coordination of glucose is in competition with coordination of a hydroxide. The formation of the rhodium−glucose complex, (**DPDE**)**Rh**^{III}(**glucose**), triggers the catalytic reaction while the coordination of hydroxides deactivates the catalyst by forming (**DPDE**)**Rh**^{III}(**OH**). The recovery of the catalyst is only possible when the inactivated (**DPDE**)**Rh**^{III}(**OH**) is reduced on the reverse scan, regenerating the (**DPDE**)**Rh**^{I} intermediate. The latter can further be oxidized and react with glucose. This phenomenon induces the reductive catalytic reactivation peak current on the reverse scan. The mechanism of activation/deactivation is depicted in Figure 6. Furthermore, the formation of the (**DPDE**)**Rh**^{III}(**glucose**) complex only occurs with deprotonated glucose (pK_a 12.8) which can then be oxidized to gluconolactone.

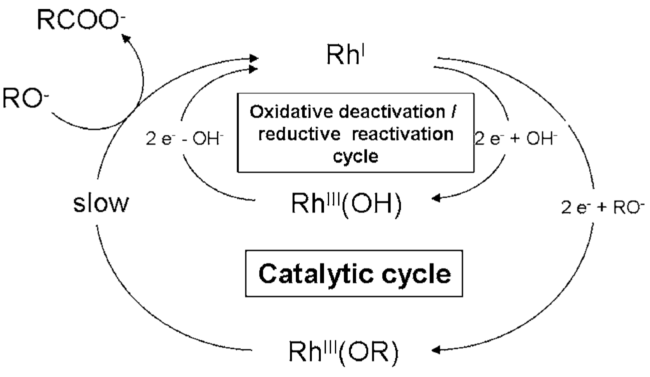

Figure 6. Oxidative deactivation and reductive activation mechanisms combined with the electrocatalytic oxidation of glucose by (**DPDE**)**Rh**^{III}. **OR** is the deprotonated form of glucose. Aqua and porphyrin ligands are omitted for clarity.

The shape of the cyclic voltammogram, as discussed by Savéant, corresponds to a mechanism of deactivation and activation occurring at narrow potentials since the same Rh(III)/Rh(I) redox couple is involved. As confirmed by theoretical calculations for a general case described by Limoges et al., the slow catalytic oxidation reaction of glucose and subsequent regeneration of the active metal center is responsible for the appearance of this electrochemical behavior. Since acid−base couples are involved in this reaction, the catalysis is strongly pH dependent (Figure S2). In fact, experiments performed at pH values inferior to 13 showed lower catalytic currents for glucose oxidation and even their disappearance at pH 8, with the deprotonated form of glucose in solution being negligible at pH values below 10 (Figure S2).

Interestingly, glucose oxidation performed by metals such as gold or platinum shows also a deactivation phenomenon that was ascribed to the competitive coordination of buffer ions and, in particular, hydroxides.[2]

4. Nonenzymatic Glucose/O_2 Fuel Cell. In order to investigate the appropriateness of (**DPDE**)**Rh**^{III} to act as a catalyst in a glucose/O_2 fuel cell, the MWCNT/(**DPDE**)**Rh**^{III} electrode was combined with a MWCNT/phthalocyanin cobalt(II) (**CoPc**) electrode as a cathode for the oxygen reduction using membrane assembly electrodes (MEAs) as represented in Figure 7A. Polarization curves for both anode and cathode are displayed in Figure S4. **CoPc** was chosen as the cathodic catalyst, due to its significantly known abilities for the oxygen reduction reaction in both acidic and basic media.[10,23,34] . The same fabrication process was employed for the creation of anode and cathode, namely the deposition of each catalyst-containing ink (1 mL) on the respective compartment of the Nafion membrane. The latter were then equipped with gold collectors before completing the fuel cell as described in the Experimental Section (Figure 7B). The MWCNT/(**DPDE**)-

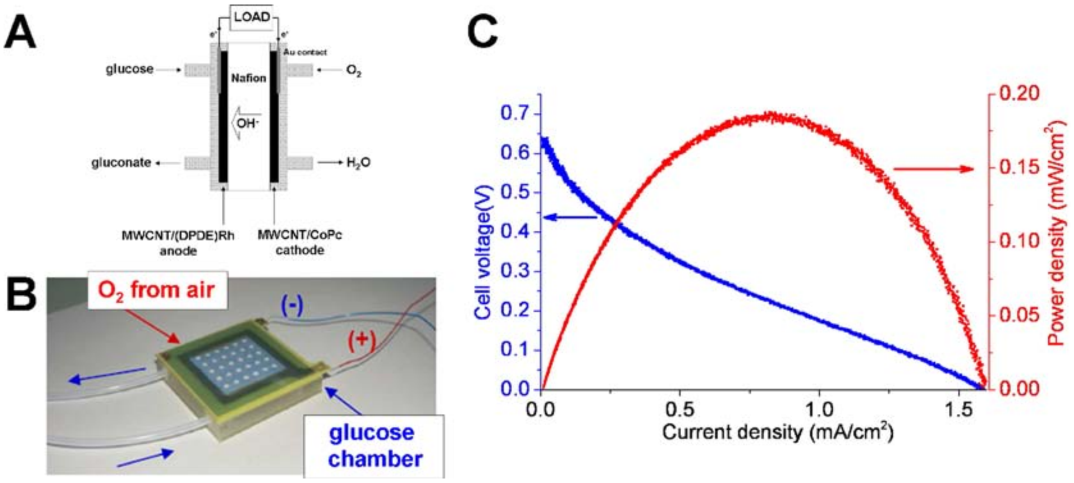

Figure 7. (A) Schematic representation of the MEA using a MWCNT/(**DPDE**)**Rh** anode and a MWCNT/**PcCo** cathode. (B) Photograph of the glucose fuel cell. (C) Polarization curve and power density curve at room temperature for a nonenzymatic glucose−O_2 fuel cell. Active area: 5.76 cm^2. Anode: MWCNT/(**DPDE**)**Rh**^{III}. Cathode: MWCNT/**PcCo**. 0.5 M of glucose, 0.5 M KOH.

Rh^{III} anode operates in a flow-through chamber that permits the anode to be constantly replenished with 0.05 M glucose at pH 14. The MWCNT/**CoPc** cathode operates at "air-breathing" conditions, i.e., direct contact of air with the cathode. Figure 7C shows the resulting fuel cell performance illustrated by a current density−voltage−power density (i−v−p) plot.

The glucose fuel cell (GFC) exhibits an OCV of 0.64 V, which is in good agreement with the sum of the potential values (0.5 V) at which the catalytic currents appear on the polarization curves recorded at pH 14, namely −0.64 V for the anode and −0.14 V for the cathode. Starting from the OCV, the cell voltage decreases until reaching a maximum (short-circuit) current density of 1.6 mA cm^{-2}. The variation of the cell power (calculated from the i−v curve) as a function of the cell voltage exhibits a dissymmetric bell shape with a maximum of 0.18 mW cm^{-2} at 0.22 V. Considering the 17-fold increase of the electroactive surface area caused by MWCNTs, a maximum power/area of 0.011 mW cm^{-2} was estimated from the estimation of the real nanostructured surface. The power curve gives access to the GFC maximum power density of 0.18 mW cm^{-2} at 0.22 V. No decrease of the fuel cell performance was observed during all measurements (~2 h). The OCV and $P_{\max}$ at room temperature have been reported to be 0.65 V and 0.22 mW cm^{-2} for alkaline FC with a silver-modified Au anode and 10 mM glucose in 0.3 M NaOH,[35] 0.385 V and 0.196 mW cm^{-2} for alkaline FC with a Ag anode and 0.8 M glucose in 1.0 M KOH,[36] and 0.86 V and 1.5 mW cm^{-2} for Nafion-based alkaline FC with a PtRu (3 mg/cm^2) anode and 0.5 M glucose in 0.5 M KOH.[1] Without considering the different experimental conditions, it appears that the performances of the molecular catalyst-based glucose/O_2 fuel cell are only slightly inferior to those of other fuel cell setups using metal or metal alloys. However, it should be noted that the molecular-catalysis fuel cell required only 0.006 mg cm^{-2} of cobalt metal and 0.011 mg cm^{-2} of Rh metal. These amounts of metal are approximately 500 times below the amount of catalytic metal necessary for the previously mentioned noble metal electrodes highlighting the advantage of the concept of molecular catalyst-based glucose/O_2 fuel cell, especially when using a non-earth-abundant metal like rhodium.

For comparison, other molecular catalyst based fuel cell delivered 7 mW cm^{-2} for direct ethanol fuel cell,[37] 24 mW cm^{-2} for direct CO PEMFC,[38] and 74.4 mW cm^{-2} for hydrogen PEMFC,[39] respectively.

■ CONCLUSION

An in depth study of the electrochemical properties of rhodium porphyrin complex and its capacity to serve as catalyst for glucose oxidation in a fuel cell setup is presented. The investigations of the intermediary oxidation sites of Rh in water at a broad pH range lead to a comprehensive understanding of the oxidation mechanism of glucose by Rh porphyrins in an alkaline solution. Furthermore, an original activation/deactivation mechanism is highlighted. The elucidation of the different pH dependent oxidation and coordination states of (**DPDE**)**Rh** gives essential information for the optimization of glucose fuel cell performances using molecular catalysts. These studies also reveal the influence of the pK_a values of (**DPDE**)**Rh** and glucose itself for efficient catalytic oxidation of the latter.

Finally, this work represents, to our knowledge, the first realization of a glucose fuel cell using uniquely molecular catalysts at both the cathode and the anode. Promisingly, the fuel cell performance, which has yet to be optimized, is on the same order of magnitude as that of existing alkaline glucose fuel cells. The modified PEMFC shows interesting performances that motivate further investment in the development of power supply derived from biofuels.

■ ASSOCIATED CONTENT

Ⓢ Supporting Information

Additional figures of chronoamperometric and cyclovoltametric measurement and polarization curves. This material is available free of charge via the Internet at http://pubs.acs.org.

■ AUTHOR INFORMATION

Corresponding Author

serge.cosnier@ujf-grenoble.fr

Notes

The authors declare no competing financial interest.

ACKNOWLEDGMENTS

The authors would like to thank the platform "Functionalization of Surfaces and Transduction" of the scientific structure "Nanobio" for providing facilities. The authors also thank the ANR P2N-2010 Program, Project GLUCOPAC, for financial support.

REFERENCES

(1) Fujiwara, N.; Yamazaki, S.-i.; Siroma, Z.; Ioroi, T.; Senoh, H.; Yasuda, K. *Electrochem. Commun.* **2009**, *11*, 390−392.
(2) Pasta, M.; La Mantia, F.; Cui, Y. *Electrochim. Acta* **2010**, *55*, 5561−5568.
(3) Holzinger, M.; Le Goff, A.; Cosnier, S. *Electrochim. Acta* **2012**, DOI: 10.1016/j.electacta.2011.12.135.
(4) Barton, S. C.; Gallaway, J.; Atanassov, P. *Chem. Rev.* **2004**, *104*, 4867−4886.
(5) Cracknell, J. A.; Vincent, K. A.; Armstrong, F. A. *Chem. Rev.* **2008**, *108*, 2439−2461.
(6) Willner, I.; Yan, Y.-M.; Willner, B.; Tel-Vered, R. *Fuel Cells* **2009**, *9*, 7−24.
(7) Gellett, W.; Kesmez, M.; Schumacher, J.; Akers, N.; Minteer, S. D. *Electroanalysis* **2010**, *22*, 727−731.
(8) Sharma, T.; Hu, Y.; Stoller, M.; Feldman, M.; Ruoff, R. S.; Ferrari, M.; Zhang, X. *Lab Chip* **2011**, *11*, 2460−2465.
(9) Basu, D.; Basu, S. *Electrochim. Acta* **2010**, *55*, 5775−5779.
(10) Morozan, A.; Jousselme, B.; Palacin, S. *Energy Environ. Sci.* **2011**, *4*, 1238−1254.
(11) Yamazaki, S.-i.; Fujiwara, N.; Takeda, S.; Yasuda, K. *Chem. Commun.* **2010**, *46*, 3607−3609.
(12) Liu, L.; Yu, M.; Wayland, B. B.; Fu, X. *Chem. Commun.* **2010**, *46*, 6353−6355.
(13) Grass, V.; Lexa, D.; Momenteau, M.; Savéant, J.-M. *J. Am. Chem. Soc.* **1997**, *119*, 3536−3542.
(14) Grass, V.; Lexa, D.; Savéant, J.-M. *J. Am. Chem. Soc.* **1997**, *119*, 7526−7532.
(15) Lexa, D.; Grass, V.; Savéant, J.-M. *Organometallics* **1998**, *17*, 2673−2676.
(16) Yamazaki, S.; Yamada, Y.; Yasuda, K. *Inorg. Chem.* **2005**, *44*, 6512−6514.
(17) Yamazaki, S.-i.; Yamada, Y.; Fujiwara, N.; Ioroi, T.; Siroma, Z.; Senoh, H.; Yasuda, K. *J. Electroanal. Chem.* **2007**, *602*, 96−102.
(18) Yamazaki, S.-i.; Yao, M.; Fujiwara, N.; Siroma, Z.; Yasuda, K.; Ioroi, T. *Chem. Commun.* **2012**, *48*, 4353−4355.
(19) Yamazaki, S.-i.; Yamada, Y.; Yasuda, K. *Inorg. Chem.* **2004**, *43*, 7263−7265.
(20) Collman, J. P.; Boulatov, R. *J. Am. Chem. Soc.* **2000**, *122*, 11812−11821.
(21) Zebda, A.; Gondran, C.; Le Goff, A.; Holzinger, M.; Cinquin, P.; Cosnier, S. *Nat. Commun.* **2011**, *2*, 370.
(22) Le Goff, A.; Artero, V.; Jousselme, B.; Tran, P. D.; Guillet, N.; Métayé, R.; Fihri, A.; Palacin, S.; Fontecave, M. *Science* **2009**, *326*, 1384−1387.
(23) Morozan, A.; Campidelli, S.; Filoramo, A.; Jousselme, B.; Palacin, S. *Carbon* **2011**, *49*, 4839−4847.
(24) Tran, P. D.; Le Goff, A.; Heidkamp, J.; Jousselme, B.; Guillet, N.; Palacin, S.; Dau, H.; Fontecave, M.; Artero, V. *Angew Chem., Int. Ed.* **2011**, *50*, 1371−1374.
(25) Zhang, W.; Shaikh, A. U.; Tsui, E. Y.; Swager, T. M. *Chem. Mater.* **2009**, *21*, 3234−3241.
(26) Zagal, J. H.; Griveau, S.; Ozoemena, K. I.; Nyokong, T.; Bedioui, F. *J. Nanosci. Nanotechnol.* **2009**, *9*, 2201−2214.
(27) Mamuru, S. A.; Ozoemena, K. I.; Fukuda, T.; Kobayashi, N.; Nyokong, T. *Electrochim. Acta* **2010**, *55*, 6367−6375.
(28) Jones, A. K.; Lamle, S. E.; Pershad, H. R.; Vincent, K. A.; Albracht, S. P. J.; Armstrong, F. A. *J. Am. Chem. Soc.* **2003**, *125*, 8505−8514.
(29) Limoges, B. Ì. t.; Savéant, J.-M. *J. Electroanal. Chem.* **2004**, *562*, 43−52.
(30) Fourmond, V.; Infossi, P.; Giudici-Orticoni, M.-T. r. s.; Bertrand, P.; Liséger, C. *J. Am. Chem. Soc.* **2010**, *132*, 4848−4857.
(31) Bramblett, A. L.; Boeckl, M. S.; Hauch, K. D.; Ratner, B. D.; Sasaki, T.; Rogers, J. W., Jr. *Surf. Interface Anal.* **2002**, *33*, 506−515.
(32) Fu, X.; Wayland, B. B. *J. Am. Chem. Soc.* **2004**, *126*, 2623−2631.
(33) Nelson, A. P.; DiMagno, S. G. *J. Am. Chem. Soc.* **2000**, *122*, 8569−8570.
(34) Li, H.; Xu, Z.; Li, K.; Hou, X.; Cao, G.; Zhang, Q.; Cao, Z. *J. Mater. Chem.* **2011**, *21*, 1181−1186.
(35) Schechner, P.; Kroll, E.; Bubis, E.; Chervinsky, S.; Zussman, E. *J. Electrochem. Soc.* **2007**, *154*, B942−B948.
(36) Jin, C.; Taniguchi, I. *Mater. Lett.* **2007**, *61*, 2365−2367.
(37) Annen, S. P.; Bambagioni, V.; Bevilacqua, M.; Filippi, J.; Marchionni, A.; Oberhauser, W.; Schönberg, H.; Vizza, F.; Bianchini, C.; Grützmacher, H. *Angew. Chem., Int. Ed.* **2010**, *49*, 7229−7233.
(38) Yamazaki, S. i.; Ioroi, T.; Yamada, Y.; Yasuda, K.; Kobayashi, T. *Angew. Chem., Int. Ed.* **2006**, *45*, 3120−3122.
(39) Brushett, F. R.; Thorum, M. S.; Lioutas, N. S.; Naughton, M. S.; Tornow, C.; Jhong, H.-R. M.; Gewirth, A. A.; Kenis, P. J. A. *J. Am. Chem. Soc.* **2010**, *132*, 12185−12187.